

3D Gaussian Splatting with Self-Constrained Priors for High Fidelity Surface Reconstruction

Takeshi Noda¹ Yu-Shen Liu^{1†} Zhizhong Han²

¹School of Software, Tsinghua University, Beijing, China

²Department of Computer Science, Wayne State University, Detroit, USA

yeth24@mails.tsinghua.edu.cn liuyushen@tsinghua.edu.cn h312h@wayne.edu

Abstract

Rendering 3D surfaces has been revolutionized within the modeling of radiance fields through either 3DGS or NeRF. Although 3DGS has shown advantages over NeRF in terms of rendering quality or speed, there is still room for improvement in recovering high fidelity surfaces through 3DGS. To resolve this issue, we propose a self-constrained prior to constrain the learning of 3D Gaussians, aiming for more accurate depth rendering. Our self-constrained prior is derived from a TSDF grid that is obtained by fusing the depth maps rendered with current 3D Gaussians. The prior measures a distance field around the estimated surface, offering a band centered at the surface for imposing more specific constraints on 3D Gaussians, such as removing Gaussians outside the band, moving Gaussians closer to the surface, and encouraging larger or smaller opacity in a geometry-aware manner. More importantly, our prior can be regularly updated by the most recent depth images which are usually more accurate and complete. In addition, the prior can also progressively narrow the band to tighten the imposed constraints. We justify our idea and report our superiority over the state-of-the-art methods in evaluations on widely used benchmarks. Project page: <https://takeshie.github.io/GSPrior/>

1. Introduction

3D Gaussian splatting (3DGS) [2] becomes a crucial tool for novel view synthesis. Learning explicit 3D Gaussian functions with attributes like color and opacity, 3DGS represents scenes as radiance fields that can be rendered into RGB images with a differentiable splatting operation. Compared with ray tracing based neural rendering methods [11, 40, 50], 3DGS shows faster rendering speed and better visual fidelity. However, it is still limited in recovering accurate geometry.

Recent works on improving accuracy of depth rendering adopts different strategies, such as reformulating rendering equations for unbiased depth inference [6, 54], imposing multi-view consistency constraints on rendered depth [1, 7, 62], constraining Gaussian movements within a distance field [3, 4], or getting supervised by additional priors from data-driven based models [24, 29, 67]. However, these strategies struggle to add constraints either directly on 3D Gaussians or adaptively in a geometry-aware manner. Without explicit 3D supervision, previous methods are limited in recovering geometry details, and rely on geometric assumptions or pretrained priors which usually do not generalize well on complex or unseen scenes, leading to artifacts and degraded geometric fidelity.

To resolve this issue, we propose a self-constrained prior to impose constraints on 3D Gaussians in a geometry-aware manner. Our prior is derived from depth maps rendered by the 3D Gaussians that are optimized in the radiance field without external knowledge. Along with the prior, we further introduce a coarse-to-fine strategy to progressively refine the prior with the most current depth rendering that turns out to be more accurate. Specifically, our prior is derived from the TSDF grid fused by depth maps, which measures the distance field around the estimated surface. In the grid, we define a band centered at the surfaces, where we remove Gaussians outside the band and impose constraints on the opacity of Gaussians within the band to better align with the current surface estimation. The geometry-aware constraints reduce the impact brought by Gaussian outliers, and make the constraints become targeted on specific Gaussians. Moreover, the refining strategy not only refines the prior but also provides a way to progressively adjust the band to tighten the imposed constraints. We conduct evaluations on widely used benchmark to justify our idea and report our superiority over the state-of-the-art methods. Our contributions are listed below,

- We propose a self-constrained prior to impose constraints on the learning of 3D Gaussians in a geometry-aware manner.

[†] Corresponding author.

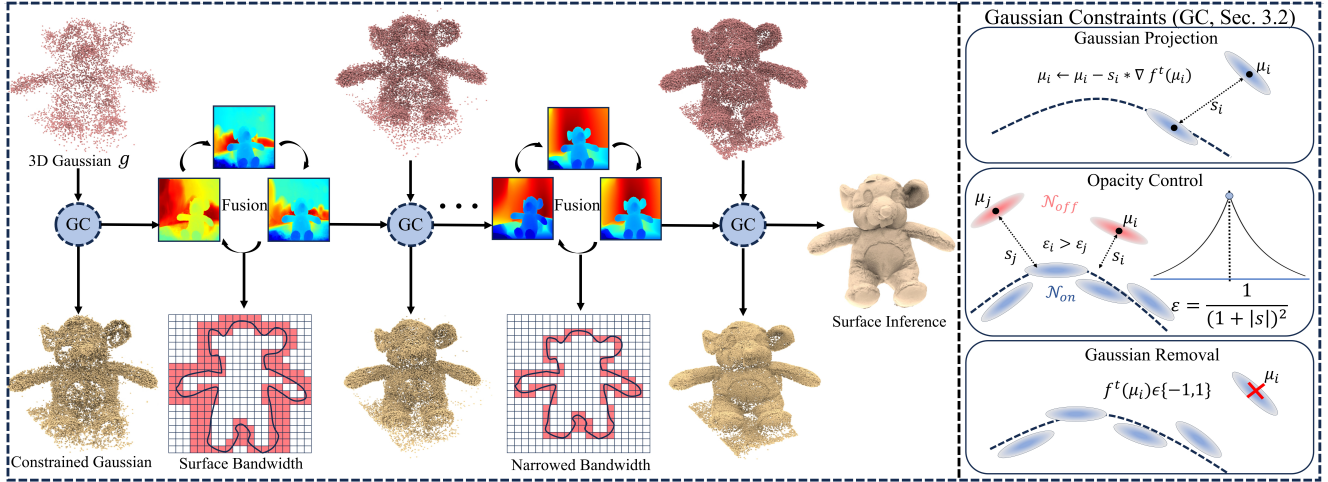


Figure 1. Overview of our method. Given 3D Gaussians g , we employ a distance field specified by a fused TSDF grid as our prior f^t . With f^t , we define a bandwidth by the surface and iteratively refine f^t with updated depth renderings. We also apply Gaussian geometric constraints (GC) that are related to interpolated distance s , centers μ and gradients ∇f^t for high fidelity surface reconstruction.

- We introduce a novel framework and losses to work with the self-constrained prior to recover more accurate geometry through 3DGS.
- We report state-of-the-art results in accuracy on the widely used benchmarks.

2. Related Work

Surface Reconstruction with Multi-view Images. Neural Radiance Fields (NeRFs) [40] have shown promising breakthroughs in novel view synthesis [3, 8, 17, 18, 21, 33] and surface reconstruction [1, 11, 15, 21, 36, 50, 66]. Previous methods model continuous density and color fields with the differentiable volume-rendering and implicit representations [36, 39, 42, 46]. With learned implicit fields, the Marching Cubes [37] algorithm is utilized to extract the zero-level-set as the surface. As data scale grows, the NeRFs based methods face significant challenges in training and inference efficiency. To address this, some studies introduce sparse or explicit grid structures [4, 14, 45], multi-resolution representations [31, 41], and geometric priors [15, 32, 48, 61, 64]. However, these strategies still struggle to balance training efficiency and reconstruction fidelity. 3DGS based methods [2, 34, 34, 43] achieves superior efficiency in novel view synthesis and geometry modeling with explicit 3D Gaussians. Recent studies [9, 12, 13, 16, 20, 52, 53, 57] further extend the framework to recover surfaces or geometries. Typically, 2DGS [20] and GSurfel [9] constrains Gaussians to 2D surfels for better surface approximation. However, these methods still struggle to recover geometry details.

Learning Gaussians with Implicit Representations. Cur-

rent Gaussian-based methods [1, 2, 9, 20, 22] construct TSDFs from depth maps but produce discontinuous surfaces at regions with complex geometry. Meanwhile, surface inference without explicit 3D constraints fails to recover accurate geometry. To solve this issue, recent studies employ implicit field representations [4, 38, 57]. GSPull [4] progressively pulls Gaussians toward object surfaces to build a continuous implicit representation. Similarly, GS-UDF [3] additionally learns an unsigned distance field (UDF) to project Gaussians with implicit surfaces for accurate reconstruction in open-surface scenarios. GOF [59] introduces a volumetric renderer explicitly models opacity and employs Marching Tetrahedra [44] for adaptive meshing. To combine the strengths of Gaussians and implicit fields, GSDF [57] jointly learns both representations and enforces mutual supervision with depth and normal cues for better reconstruction. However, the joint optimization strategy requires a differentiable formulation between the radiance field and the implicit function, which complexes the framework.

Inferring Surfaces through 3DGS. Enhancing geometry through priors has been widely explored in recent studies [6, 19, 28, 29, 29, 47, 52, 53, 60]. PGSR [1] incorporates multi-view constraints to improve both rendering quality and geometric fidelity. However, local over-smoothing is observed in the reconstructed surfaces, as the 3D Gaussians are not sufficiently constrained by image-based supervision. To further enhance reconstruction, some methods introduce geometric priors for supervision. DN-Splatter [47] leverages depth and normal priors as geometric constraints during optimization. Similarly, SuGaR [19] builds density fields with a regularization term to align Gaussians with the scene and extracts surfaces via Poisson reconstruction [25]. However, geometric and implicit field priors gen-

erally provide supervision with different scales and require additional optimization for alignment.

Different from all these methods, our method introduces a prior that can be derived from the depth maps to directly impose constraints on 3D Gaussians in a geometry-aware manner. The coarse-to-fine refining can progressively produce a better prior to constrain Gaussians adaptively, eventually achieving more accurate depth rendering.

3. Method

Overview. Our method is illustrated in Fig. 1. We aim to learn a set of 3D Gaussians $\{g_j\}_{j=1}^J$ from I images $\{v_i\}_{i=1}^I$ for high fidelity surface reconstruction. With the learned Gaussians $\{g_j\}$, we can render $\{g_j\}$ into depth maps $\{d'\}$ and fuse them into a TSDF for surface extraction, or RGB images $\{v'_i\}$ for novel view synthesis. The key of our method is a self-constrained prior which constrains the learning of 3D Gaussians without data-driven priors for more accurate depth rendering. Our prior does not need an additional learning, and can provide a distance field to impose more specific constraints on 3D Gaussians. For instance, we can remove outlier Gaussians, encourage larger opacity for Gaussians that are close to surfaces or smaller opacity for Gaussians that are far away from surfaces, and move Gaussians nearer to surfaces. Meanwhile, we will regularly update the prior with the most recent rendered depth maps which are more accurate in surface estimation. Additionally, we will shrink the range of area around estimated surfaces each time to progressively impose tightened constraints on the learning of Gaussians.

3.1. Learning Self-Constrained Priors

RGB and Depth Rendering. With a set of 3D Gaussians $\{g_j\}$, we first render $\{g_j\}$ into a depth map d'_i from a specific view p_i through a splatting procedure \mathcal{S} ,

$$d'_i = \mathcal{S}(\{g_j\}, \{z_{ji}\}, p_i), \quad (1)$$

where z_{ji} is the Z coordinate of Gaussian g_j in the camera coordinate system specified by p_i . Similarly, we can render $\{g_j\}$ into an RGB image by alpha blending with color c_j . i.e., $v'_i = \mathcal{S}(\{g_j\}, \{c_j\}, p_i)$.

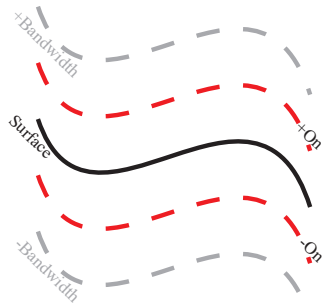


Figure 2. Illustration of bandwidth and the range of opacity control.

It is obtained by fusing depth maps rendered at iteration t with

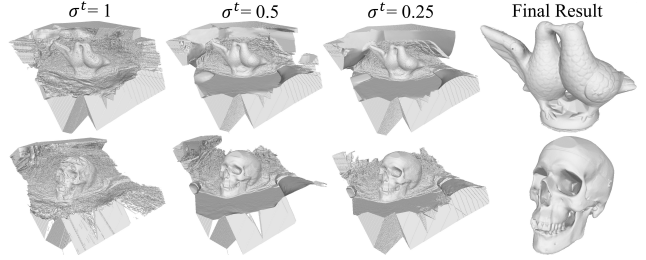


Figure 3. Visualization of periodical update on our prior.

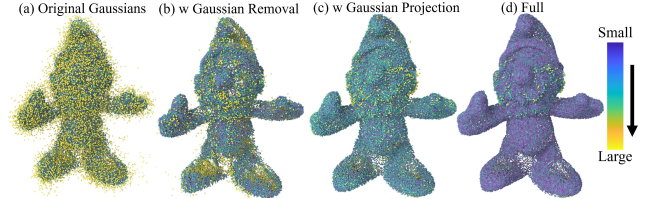


Figure 4. Visualization of Gaussian centers with each constraint. The error map indicates the distance to the ground truth surface.

the depth fusion operation \mathcal{F} ,

$$f^t = \mathcal{F}(\{d'_i(t)\}). \quad (2)$$

With the distance field f^t , we can regard the zero-level set as a coarse surface estimation, which provides a reference to work with the learning of Gaussians in return. As shown in Fig. 2, beyond the zero-level set, we focus on a narrow band by the surface, which spans a distance field from -1 to 1 . We can use a threshold σ^t to control the truncation distance at iteration t , which determines the width of the narrow band.

Periodic Update. We update the distance field f^t at regular intervals with the most recent rendered depth maps to improve the coarse surface estimation and balance the additional computation for depth fusion as well. Since the most recent rendered depth maps are more multi-view consistent and accurate, the updated prior can impose more specific constraints on Gaussians and benefit the learning of Gaussians. Moreover, we also progressively reduce the width of the narrow band to strengthen the constraints along with stabilizing the optimization. We show the updated fields f^t with different truncation distances threshold σ^t in Fig. 3.

3.2. Constraints with a Self-Constrained Prior

Removal of Gaussian Outliers. Once we have a distance field f^t , we can remove the Gaussians that are outside the narrow band as specified in Fig. 2. We aim for a more compact Gaussian distribution so that the rendered depth can get less negative impact of Gaussian outliers that are far away from the surface estimation. Specifically, we interpolate the signed distance s_j at the center μ_j of each Gaussian g_j from the field f^t using the trilinear interpolation, i.e.,

$s_j = f^t(\mu_j)$. If the interpolated s_j is either 1 or -1 , we regard this Gaussian as an outlier and remove it from the Gaussian set. Fig. 4 (b) shows Gaussian removal can significantly reduce the impact brought by Gaussian outliers.

Constraints on Opacity. Although the field f^t remains an estimation, it is adequate to present a coarse surface inference. Unlike the previous methods [38, 59] that directly learn a mapping from SDFs to opacity, we encourage opacity to be maximal on the surface estimation and minimal at the band boundary. Thus, we split all Gaussians within the band into two subsets, one is the on-surface subset \mathcal{N}_{on} , the other is off-surface subset \mathcal{N}_{off} , as illustrated by the range of the two subsets in Fig. 2. We use a signed distance threshold δ^t to label each Gaussian into one of the two subsets, where we interpolate the s_j of each Gaussian from f^t , we have $\mathcal{N}_{on} = \{g_j | |s_j| \leq \delta^t\}$, $\mathcal{N}_{off} = \{g_j | \delta^t < |s_j| \leq 1\}$. Therefore, the constraint on opacity is formulated as,

$$L_{SCP} = \frac{1}{M} \left(\sum_{g_k \in \mathcal{N}_{on}} \varepsilon_k (o_k - 1)^2 + \sum_{g_{k'} \in \mathcal{N}_{off}} \varepsilon_{k'} o_{k'}^2 \right), \quad (3)$$

where o is the opacity of Gaussian g , M is the total number of Gaussians. Both ε_k and $\varepsilon_{k'}$ are weights for the importance of each sample, according to its interpolated distance to the surface, which is formulated as $\varepsilon_j = 1/(1 + |s_j|)^2$.

Moving Toward Surfaces. Within the band, we leverage the signed distance field f^t to move all Gaussians toward the surface. Fig. 4 (c) shows that the pulling can move most of Gaussians in Fig. 4 (a) closer to surfaces. We leverage the interpolated signed distances and gradients to project all Gaussians onto the surface. Unlike previous methods [3, 4], we do not involve the pulling into the iterative optimization for stabilizing the optimization. Instead, we regard the projection as an update of Gaussian positions. For each Gaussian g_j , we first interpolate the signed distance s_j at the center μ_j , and calculate its gradient $\nabla f^t(\mu_j)$ using finite difference in the grid-based field f^t ,

$$\nabla f^t(\mu_j) = \frac{1}{2\epsilon} \begin{bmatrix} f^t(x_j + \epsilon, y_j, z_j) - f^t(x_j - \epsilon, y_j, z_j) \\ f^t(x_j, y_j + \epsilon, z_j) - f^t(x_j, y_j - \epsilon, z_j) \\ f^t(x_j, y_j, z_j + \epsilon) - f^t(x_j, y_j, z_j - \epsilon) \end{bmatrix}, \quad (4)$$

where ϵ denotes the displacement which gets set to 1×10^{-4} , and $\mu_j = [x_j, y_j, z_j]$. With the interpolated signed distance s_j and the gradient $\nabla f^t(\mu_j)$, we update the position by

$$\mu_j \leftarrow \mu_j - s_j * \nabla f^t(\mu_j). \quad (5)$$

Constraint Scheduling. We schedule these constraints within 3DGS. We impose the opacity constraint in each iteration, and apply pulling and then outlier removal strategies after each densification. With densified Gaussians, we first pull all Gaussians toward the surface using Eq. 5, and then remove the Gaussians outliers that are still outside the band. Fig. 4 (d) illustrates the Gaussians with all constraints.

3.3. Loss Functions

We use planar Gaussians in 3DGS for better geometry representation. Besides, the constraint on opacity with our self-constrained prior in Eq. 3, we also use loss terms to evaluate the RGB rendering errors and multi-view consistency on depth maps. Specifically, we use L_{RGB} to evaluate the error of rendering v' to the input image v with a mean absolute error (MAE), a structural similarity (SSIM), and the multi-view normalized cross correlation (NCC).

Based on that, to learn a consistent surface from multi-view depth maps, we also leverage L_{Depth} to make the per-ray depth distribution thinner and more consistent,

$$L_{Depth} = \sum_{u=0}^{U-1} \sum_{u'=0}^{u-1} \omega_u \omega_{u'} (\rho_u - \rho_{u'})^2, \quad (6)$$

where $\{\omega_u, \omega_{u'}\}$ is the alpha-blending weights of the Gaussian, ρ_u is the intersection depth, U is the count of Gaussian on a ray, u and u' index the Gaussians along the ray.

To align Gaussians with actual surface, we introduce a normal regularization for accurate geometry approximation. We first employ L_{NS} to evaluate the consistency between the rendered normal n_i and the derived normal n'_i from rendered depth,

$$L_{NS} = \frac{1}{|I|} \sum_{i \in I} \eta_k \|n_i - n'_i\|_1, \quad (7)$$

where $\eta_k = (1 - \|\nabla I\|)^2$ serves as per-pixel weights. However, L_{NS} struggles to ensure the alignment of local details and tends to smooth the global shape.

To address this, we incorporate cross-view consistency with the homography matrix H_{rm} to align local geometry between the reference view r and the neighboring view m ,

$$H_{rm} = C_m \left(R_{rm} + \frac{T_{rm} n_r^\top}{\tau_r} \right) C_r^{-1}, \quad (8)$$

where $\{C_r, C_m\}$ are camera intrinsics, R_{rm} and T_{rm} are relative rotation and translation, n_r is the plane normal in r , and τ_r is the plane distance in reference camera coordinates. Therefore, we constrain the geometry consistency with L_{NM} below,

$$L_{NM} = \frac{1}{|V|} \sum_{p_r \in V} \|h_r - H_{mr} H_{rm} h_r\|_1, \quad (9)$$

where V denotes the set of valid pixels in r , h_r is the homogeneous pixel coordinate in r , and $\{H_{mr}, H_{rm}\}$ are the homography matrices.

Overall, we minimize the loss function L by,

$$L = L_{RGB} + \lambda_1 L_{Depth} + \lambda_2 L_{NS} + \lambda_3 L_{NM} + \lambda_4 L_{SCP}, \quad (10)$$

where $\{\lambda_1, \lambda_2, \lambda_3, \lambda_4\}$ are the balance weights, and we set them as $\lambda_1 = 0.01$, $\lambda_2 = 0.1$, $\lambda_3 = 0.1$, and $\lambda_4 = 0.01$.

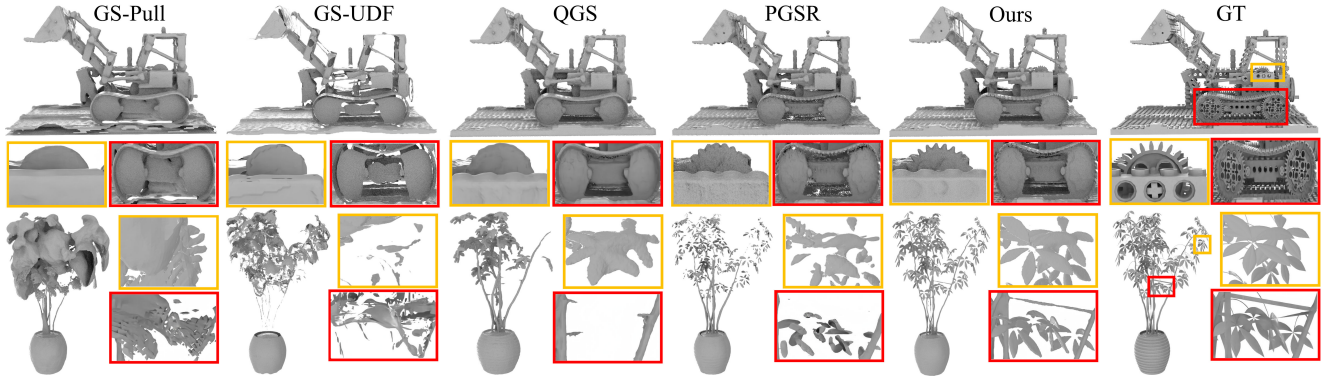


Figure 5. Visual comparison of reconstruction on NeRF-Synthetic dataset.

4. Experiments

4.1. Experiment Setup

Datasets and Metrics. We evaluate our method on four datasets with synthetic and real scanned scenes, including: NeRF-Synthetic [40], DTU [23], Tanks and Temples (TNT) [27], and Mip-NeRF 360 [2]. For NeRF-Synthetic, we report the L1 Chamfer Distance (CD_{L1}) between the ground-truth point cloud and the predicted surface. Meanwhile, we report PSNR for view accuracy. For DTU, we also analyze the performance in geometry inference and image rendering with CD and PSNR. For TNT, we report the F1-score to measure the alignment between the predicted surface and the ground-truth point cloud. For Mip-NeRF 360, we employ PSNR, SSIM, and LPIPS as evaluation metrics for large-scale novel view synthesis. We follow 2DGS to extract surfaces with TSDF-Fusion under the same settings.

Baselines. We compare our method with state-of-the-art methods with different learning strategies, including methods with explicit representations [2, 4, 9, 20, 38, 57, 59], implicit representations [2, 10, 31, 40, 41, 49, 51, 55, 56], and various constraints [1, 3, 9, 19, 47]. We evaluate the performance in reconstruction and rendering under the same settings.

4.2. Results and Evaluation

Comparisons on NeRF-Synthetic. We first evaluate our method on synthetic scenes and present quantitative and visual comparisons in Tab. 1, Fig. 5, and Fig. 6, respectively. As reported in Tab. 1, our method outperforms all baselines in both CD and PSNR metrics. We further present geometry comparison results in Fig. 5. PGSR [1] enforces multi-view consistency but still struggles to recover complete geometric details and complex structures. In contrast, our method leverages depth cues and 3D geometric constraints within the implicit field to achieve more complete geometry. Meanwhile, different from GS-Pull [4] and GS-UDF [3] that fit 3D Gaussians with gradients to learn implicit fields,

Table 1. Quantitative comparisons in terms of CD_{L1} ($\times 100$) and PSNR on the NeRF-Synthetic dataset.

Class	Method	$CD_{L1} (\times 100) \downarrow$	PSNR \uparrow
Implicit	NeuS [49]	2.33	30.20
	NeRO [35]	1.92	27.48
	VolSDF [55]	2.86	27.96
Explicit	2DGS [20]	2.26	33.07
	GS-UDF [3]	2.25	33.37
	GS-Pull [4]	2.31	33.29
	PGSR [1]	2.18	34.05
	QGS [5]	2.04	30.41
	Ours	1.87	34.21

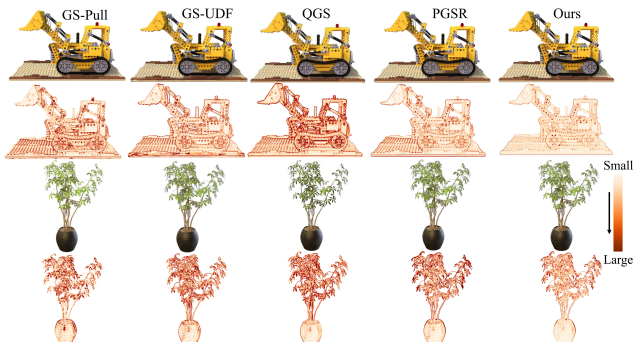


Figure 6. Error map comparison of rendering on NeRF-Synthetic.

our method extracts stable implicit priors from depth maps for more stable geometry inference. The comparisons of error maps on renderings in Fig. 6 also demonstrate that our method produces smaller errors in challenging regions.

Comparisons on DTU. We also validate our method on the real-scanned dataset compared with state-of-the-art approaches. As shown in Tab. 2, our method achieves the best results across scenes. Compared with implicit methods, our method does not need to learn SDF or priors, which balances both accuracy and efficiency. 2DGS [20] and QGS [5] apply 2D normal regularization to smooth surfaces. However, 2D priors are insufficient for accurate surface reconstruction, leading artifacts in challenging regions. GOF [59]

Table 2. Quantitative comparisons in terms of CD on the DTU dataset.

Class	Methods	24	37	40	55	63	65	69	83	97	105	106	110	114	118	122	Mean	Time
Implicit	NeRF [40]	1.90	1.60	1.85	0.58	2.28	1.27	1.47	1.67	2.05	1.07	0.88	2.53	1.06	1.15	0.96	1.49	>12h
	VolSDF [55]	1.14	1.26	0.81	0.49	1.25	0.70	0.72	1.29	1.18	0.70	0.66	1.08	0.42	0.61	0.55	0.86	>12h
	NeuS [49]	1.00	1.37	0.93	0.43	1.10	0.65	0.57	1.48	1.09	0.83	0.52	1.20	0.35	0.49	0.54	0.84	>12h
	Neuralangelo [31]	0.37	0.72	0.35	0.35	0.87	0.54	0.53	1.29	0.97	0.73	0.47	0.74	0.32	0.41	0.43	0.61	>12h
	NeuralWarp [10]	0.49	0.71	0.38	0.38	0.79	0.82	0.82	1.20	1.06	0.68	0.66	0.74	0.41	0.63	0.51	0.68	>10h
Explicit	2DGS [20]	0.48	0.91	0.39	0.39	1.01	0.83	0.81	1.36	1.27	0.76	0.70	1.40	0.40	0.76	0.52	0.80	19.2min
	GS-Pull [4]	0.51	0.56	0.46	0.39	0.82	0.67	0.85	1.37	1.25	0.73	0.54	1.39	0.35	0.88	0.42	0.75	22min
	GS-UDF [3]	0.62	0.67	0.43	0.42	0.83	0.86	0.72	1.20	1.03	0.68	0.61	0.63	0.43	0.56	0.52	0.68	25min
	SuGaR [19]	1.47	1.33	1.13	0.61	2.25	1.71	1.15	1.63	1.62	1.07	0.79	2.45	0.98	0.88	0.79	1.33	1h
	GOF [59]	0.50	0.82	0.37	0.37	1.12	0.74	0.73	1.18	1.29	0.68	0.77	0.90	0.42	0.66	0.49	0.74	1h
	PGSR [1]	0.34	0.58	0.29	0.29	0.78	0.58	0.54	1.01	0.73	0.51	0.49	0.69	0.30	0.35	0.38	0.53	40min
	GSDF [57]	0.58	0.93	0.46	0.37	1.30	0.77	0.73	1.58	1.28	0.76	0.58	1.22	0.37	0.51	0.51	0.80	32min
	QGS [5]	0.38	0.62	0.37	0.38	0.75	0.55	0.51	1.12	0.68	0.61	0.46	0.58	0.35	0.41	0.40	0.54	48min
	Ours	0.32	0.55	0.30	0.31	0.74	0.54	0.48	1.06	0.69	0.57	0.45	0.58	0.29	0.35	0.33	0.50	42min

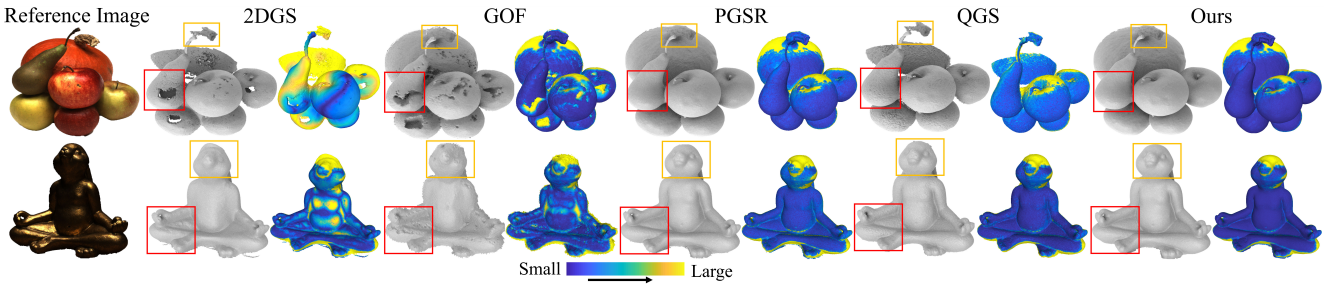


Figure 7. Visual comparison of reconstruction on DTU dataset. The error map indicates the distance to the ground truth surface.

Table 3. Quantitative comparisons in terms of F1-Score on the TNT dataset.

Class	Methods	Barn	Caterpillar	Courthouse	Ignatius	Meetingroom	Truck	Mean
Implicit	NeuS [49]	0.29	0.29	0.17	0.83	0.24	0.45	0.38
	Geo-NeuS [15]	0.33	0.26	0.12	0.72	0.20	0.45	0.35
	Neuralangelo [31]	0.70	0.36	0.28	0.89	0.32	0.48	0.50
	MonoSDF [58]	0.49	0.31	0.12	0.78	0.23	0.42	0.39
Explicit	3DGS [2]	0.13	0.08	0.09	0.04	0.01	0.19	0.09
	SuGaR [19]	0.14	0.16	0.08	0.33	0.15	0.26	0.19
	GSurfields [9]	0.24	0.22	0.07	0.39	0.12	0.24	0.21
	2DGS [20]	0.36	0.23	0.13	0.44	0.16	0.26	0.30
	PGSR [1]	0.66	0.41	0.21	0.80	0.29	0.60	0.50
	GOF [59]	0.51	0.41	0.28	0.68	0.28	0.59	0.46
	GS-Pull [4]	0.60	0.37	0.16	0.71	0.22	0.52	0.43
	QGS [5]	0.55	0.40	0.28	0.81	0.31	0.64	0.50
	Ours	0.66	0.43	0.20	0.80	0.31	0.64	0.51

Table 4. Quantitative comparisons in terms of PSNR, SSIM and LPIPS on the Mip-NeRF 360 dataset.

Class	Method	Outdoor Scenes			Indoor Scenes		
		PSNR \uparrow	SSIM \uparrow	LPIPS \downarrow	PSNR \uparrow	SSIM \uparrow	LPIPS \downarrow
Implicit	NeRF [40]	21.46	0.458	0.515	26.84	0.790	0.370
	Ins-NGP [41]	22.90	0.566	0.371	29.15	0.880	0.216
	BakedSDF [56]	22.47	0.585	0.349	27.06	0.836	0.258
	Mip-NeRF 360 [2]	24.47	0.691	0.283	31.72	0.917	0.180
Explicit	3DGS [2]	24.64	0.731	0.234	30.41	0.920	0.189
	SuGaR [19]	22.93	0.629	0.356	29.43	0.906	0.225
	2DGS [20]	24.34	0.717	0.246	30.40	0.916	0.195
	GS-Pull [4]	23.76	0.703	0.278	30.78	0.925	0.182
	GOF [59]	24.82	0.750	0.202	30.79	0.924	0.184
	PGSR [1]	24.45	0.730	0.224	30.41	0.930	0.161
	QGS [5]	24.32	0.706	0.242	30.45	0.919	0.184
	Ours	24.81	0.754	0.200	30.56	0.933	0.155

combines Gaussians with opacity fields to improve performance, but constrained by complex opacity modeling. As shown in Fig. 7, PGSR [1] further integrates multi-view consistency constraints to infer more accurate surfaces, but it still struggles to recover local details. Unlike these methods, our method extracts geometric cues directly from 2D depth maps and produces more detailed and continuous surfaces.

Comparisons on TNT. We evaluate the robustness of our method on large-scale scenes in Tanks and Temples (TNT) dataset. Tab. 3 shows that our method achieves the best reconstruction performance among all baselines. GS-Pull [4] relies on Gaussian positions for geometry inference, it is still hard to maintain all Gaussians on surfaces when learning large-scale implicit representations. Similarly, GOF [59] employs tetrahedral grids to infer complete surfaces. However, the opacity modeling limits grid optimization in large-scale dataset, leading to uneven surfaces and coarse local details. In contrast, our method reconstructs complete surfaces under complex topology using only depth cues and self-supervised geometric constraints, which effectively detect artifacts and improves efficiency. We further provide visual comparisons in Fig. 8. QGS [5] and GS-Pull [4] constrain Gaussians to lie on the surface with regularization terms and implicit field gradients, respectively. However, QGS produces artifacts due to inaccu-

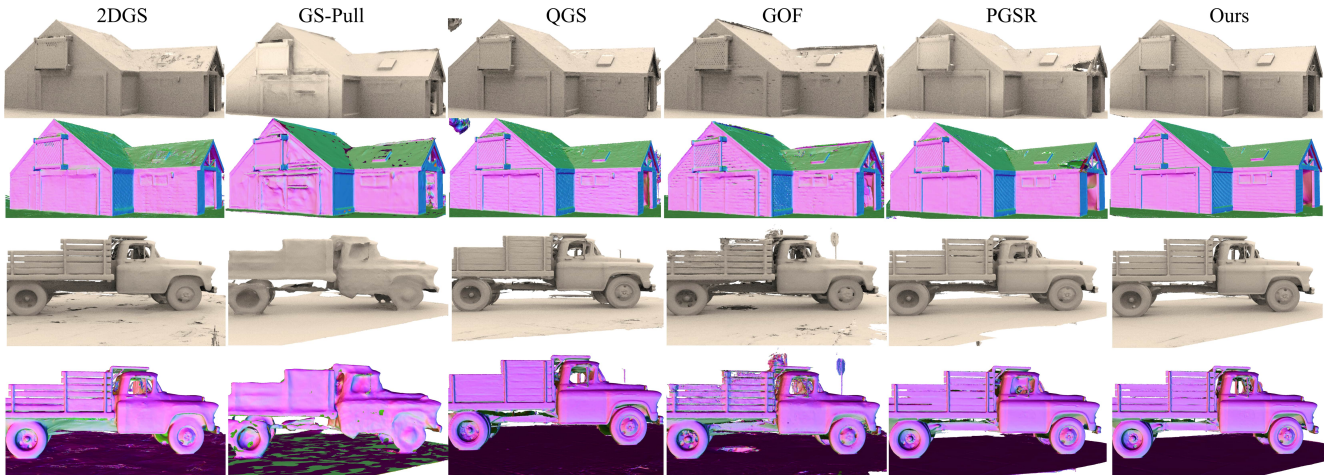


Figure 8. Visual comparison of reconstruction on TNT dataset, the color indicates the normal direction.

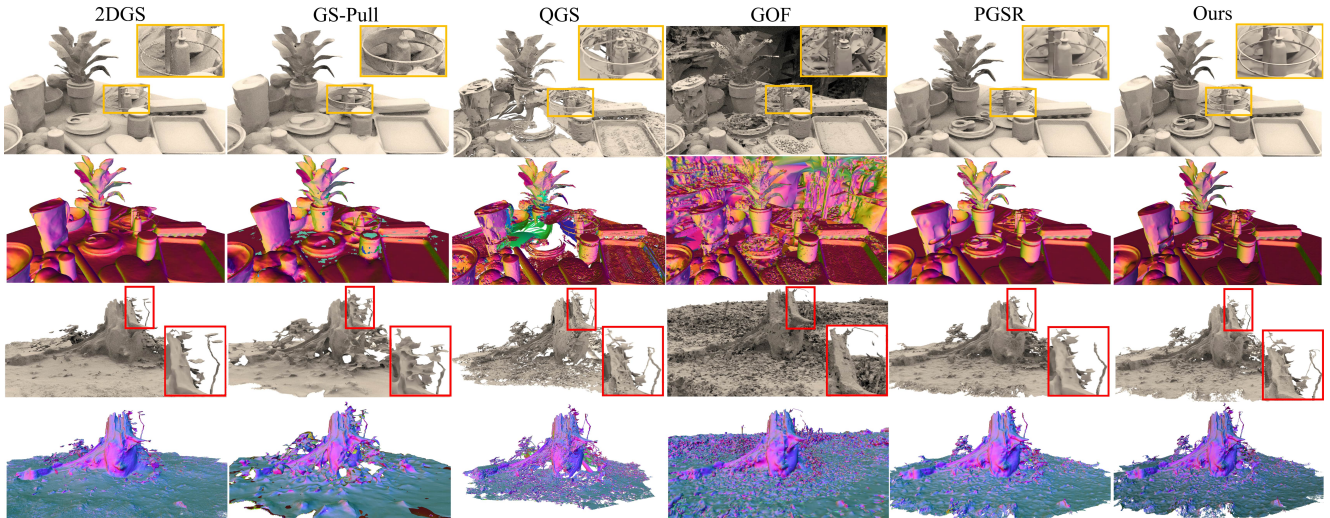


Figure 9. Visual comparison of reconstruction on Mip-NerF 360 dataset, the color indicates the normal direction.

rate surface alignment, while GS-Pull loses local details and exhibits normal errors caused by gradient noise. In contrast, our method leverages a stable implicit field to guide Gaussians toward the surface and produces more continuous and smoother surfaces.

Comparisons on Mip-NeRF 360. We further evaluate our method on the Mip-NeRF 360 dataset to validate the performance in novel view synthesis. Tab. 4 presents quantitative comparisons with both explicit and implicit methods. Our method outperforms all baselines in most metrics. Although surfel based or geometry constraints based methods perform well in geometry inference, the rendering performance is worse than 3DGS due to the impact of strict geometry constraints on Gaussian movement. As shown in Fig. 9, GOF[59] and GS-Pull [4] achieve high completeness on surfaces but struggle to recover local details in in-

door scenes. PGSR [1] and QGS [5] suffer from local truncations and artifacts due to truncated distance fields, especially in complex outdoor scenes where multi-view supervision alone struggle to maintain surface continuity on textured regions. In contrast, our method aligns Gaussians near the depth rendered surfaces to preserve the rendering fidelity and reconstruction details.

5. Ablation Studies

To validate the effectiveness of each module on DTU, we evaluate quantitative and visual analyses in Tab. 5.

Self-constrained Priors. We first evaluate the effect of the prior f^t . When we remove f^t (denoted as w/o f^t), we lose the reference to impose constraints. As shown in Tab. 5 (“Self-constrained Priors”), the lack of f^t leads to a no-

Table 5. Ablation studies on DTU dataset.

Methods	Self-constrained Priors		Opacity Constraints		Supervision Refinement			Constraints on Gaussians			Bandwidth Scales			
	w f^t	w/o f^t	w L_{SCP}	w/o L_{SCP}	$\{f_0^t\}$	$\{f_0^t, f_1^t\}$	$\{f_0^t, f_1^t, f_2^t\}$	w/o f_{remove}^t	w/o f_{proj}^t	Full	1	0.5	0.25	Full
CD↓	0.50	0.56	0.50	0.53	0.54	0.52	0.50	0.53	0.51	0.50	0.54	0.53	0.51	0.50

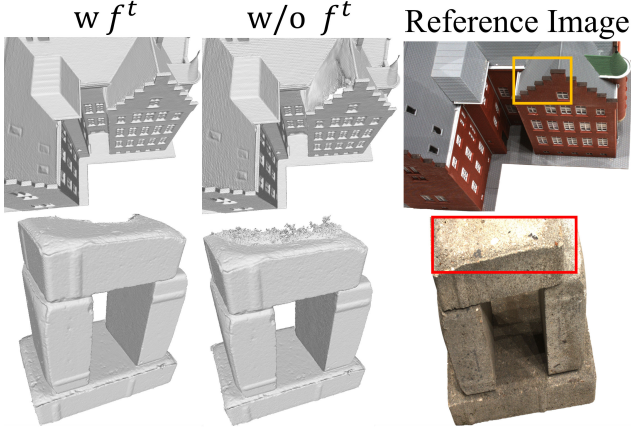


Figure 10. Effect of the self-constrained prior.

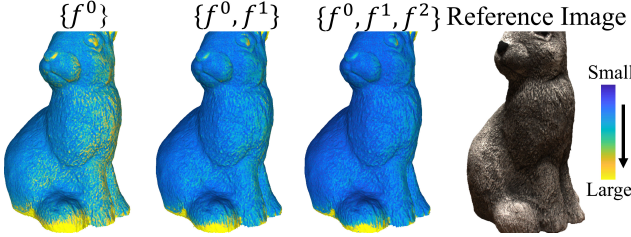


Figure 11. Effect of periodical update on our prior.

ticeable increase in CD. Visual results in Fig. 10 further demonstrate that learning Gaussian representations with f^t produces more continuous and accurate surfaces.

Prior Update. We also assess the effect of prior update on reconstruction performance. We set f^0 as baseline, which is the initial prior. Meanwhile, we update f^t from f^0 to f^2 for evaluation. As shown in Tab. 5 (“Prior Update”), CD error decreases as f^t is progressively updated. Furthermore, Fig. 11 shows that f^t guides the Gaussians to recover more continuous and detailed geometry with periodic refinement.

Constraints on Gaussians. We further analyze the effect of Gaussian constraints. As shown in Tab. 5 (“Constraints on Gaussians”), we first remove the Gaussian projection (w/o f_{proj}^t), which leads CD to increase a bit. We further disable the Gaussian removal (f_{remove}^t) and the performance gets worse. As shown in Fig. 4 and Fig. 12, the 3D Gaussians struggle to move toward the surfaces without f_{proj}^t , while f_{remove}^t helps 3D Gaussians produce continuous surfaces and removes artifacts beyond the bandwidth.

Opacity Constraints. To validate the effect of the opac-

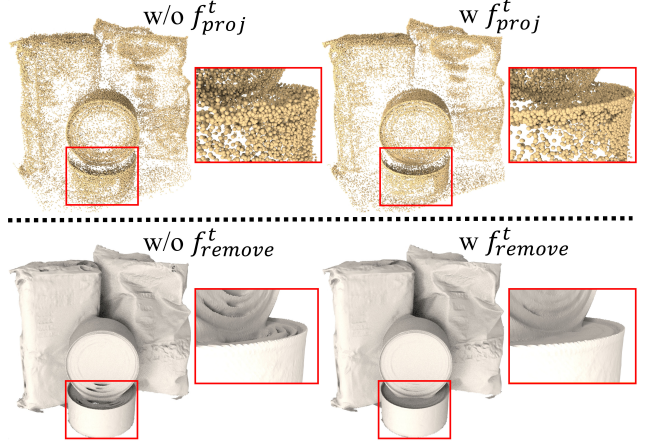


Figure 12. Effect of Gaussian Removal and Projection.

ity arrangement term L_{SCP} , we remove it (denoted as w/o L_{SCP}) and optimize the Gaussian opacities only with 2D supervisions. As shown in Tab. 5 (“Opacity Constraints”), removing L_{SCP} leads to degraded reconstruction. Although learning with multi-view constraints can recover the global shapes, but 2D constraints struggle to capture local details with complex geometry.

Bandwidth Sizes. To evaluate the effect of the bandwidth shrinking strategy, we compare a fixed bandwidth with progressively decreased thresholds $\sigma^t = 1, 0.5, 0.25$. As shown in Fig. 3, a narrower bandwidth allows f^t to capture more accurate geometric distributions and also impose more compact constraints on Gaussians. Tab. 5 further shows that the CD error decreases as the bandwidth becomes tighter, and the threshold reduction from 1 to 0.25 (Full) achieves the best performance.

6. Conclusion

We present self-constrained priors to recover high fidelity surfaces with 3DGS. We show that a self-constrained prior can be easily obtained by fusing rendered depth images without other information. With the prior, we can effectively impose constraints on specific Gaussians including the removal of outlier Gaussians, opacity control, and move Gaussians closer to the surface. Moreover, periodically update the prior also helps stabilize the optimization and progressively approach convergence. Our evaluations justified our design and show advantages over the latest methods.

7. Acknowledgment

This work was partially supported by Deep Earth Probe and Mineral Resources Exploration — National Science and Technology Major Project (2024ZD1003405), and the National Natural Science Foundation of China (62272263, W2542037).

References

- [1] Dejan Azinović, Ricardo Martin-Brualla, Dan B Goldman, Matthias Nießner, and Justus Thies. Neural RGB-D surface reconstruction. In *Proceedings of the IEEE/CVF Conference on Computer Vision and Pattern Recognition*, pages 6290–6301, 2022. 2
- [2] Jonathan T Barron, Ben Mildenhall, Dor Verbin, Pratul P Srinivasan, and Peter Hedman. Mip-NeRF 360: Unbounded anti-aliased neural radiance fields. In *Proceedings of the IEEE/CVF conference on computer vision and pattern recognition*, pages 5470–5479, 2022. 5, 6
- [3] Ang Cao and Justin Johnson. HexPlane: A fast representation for dynamic scenes. In *Proceedings of the IEEE/CVF Conference on Computer Vision and Pattern Recognition*, pages 130–141, 2023. 2
- [4] Anpei Chen, Zexiang Xu, Andreas Geiger, Jingyi Yu, and Hao Su. TensorRF: Tensorial radiance fields. In *European Conference on Computer Vision (ECCV)*, pages 333–350. Springer, 2022. 2
- [5] Danpeng Chen, Hai Li, Weicai Ye, Yifan Wang, Weijian Xie, Shangjin Zhai, Nan Wang, Haomin Liu, Hujun Bao, and Guofeng Zhang. PGSR: Planar-based gaussian splatting for efficient and high-fidelity surface reconstruction. *IEEE Transactions on Visualization and Computer Graphics*, 2024. 1, 2, 5, 6, 7
- [6] Hanlin Chen, Fangyin Wei, Chen Li, Tianxin Huang, Yunsong Wang, and Gim Hee Lee. VCR-Gaus: View Consistent Depth-Normal Regularizer for Gaussian Surface Reconstruction. *Advances in Neural Information Processing Systems*, 37:139725–139750, 2024. 1, 2
- [7] Yuedong Chen, Haoifei Xu, Chuanxia Zheng, Bohan Zhuang, Marc Pollefeys, Andreas Geiger, Tat-Jen Cham, and Jianfei Cai. MVSplat: Efficient 3D gaussian splatting from sparse multi-view images. In *European Conference on Computer Vision*, pages 370–386. Springer, 2024. 1
- [8] Zhiqin Chen, Thomas Funkhouser, Peter Hedman, and Andrea Tagliasacchi. MobileNeRF: Exploiting the polygon rasterization pipeline for efficient neural field rendering on mobile architectures. In *Proceedings of the IEEE/CVF Conference on Computer Vision and Pattern Recognition*, pages 16569–16578, 2023. 2
- [9] Pinxuan Dai, Jiamin Xu, Wenxiang Xie, Xinguo Liu, Huamin Wang, and Weiwei Xu. High-Quality surface reconstruction using gaussian surfels. In *ACM SIGGRAPH 2024 Conference Papers*, pages 1–11, 2024. 2, 5, 6
- [10] François Darmon, Bénédicte Bascle, Jean-Clément Devaux, Pascal Monasse, and Mathieu Aubry. Improving neural implicit surfaces geometry with patch warping. In *Proceedings of the IEEE/CVF Conference on Computer Vision and Pattern Recognition*, pages 6260–6269, 2022. 5, 6
- [11] Kangle Deng, Andrew Liu, Jun-Yan Zhu, and Deva Ramanan. Depth-Supervised NeRF: Fewer views and faster training for free. In *Proceedings of the IEEE/CVF Conference on Computer Vision and Pattern Recognition*, pages 12882–12891, 2022. 1, 2
- [12] Juntong Fang, Zequn Chen, Weiqi Zhang, Donglin Di, Xuancheng Zhang, Chengmin Yang, and Yu-Shen Liu. More: Motion-aware feed-forward 4D reconstruction transformer. *Conference on Computer Vision and Pattern Recognition*, 2026. 2
- [13] Xianze Fang, Jingnan Gao, Zhe Wang, Zhuo Chen, Xingyu Ren, Jiangjing Lyu, Qiaomu Ren, Zhonglei Yang, Xiaokang Yang, Yichao Yan, and Chengfei Lyu. Dens3R: A foundation model for 3D geometry prediction. 2025. 2
- [14] Sara Fridovich-Keil, Alex Yu, Matthew Tancik, Qinhong Chen, Benjamin Recht, and Angjoo Kanazawa. Plenoxels: Radiance fields without neural networks. In *Proceedings of the IEEE/CVF Conference on Computer Vision and Pattern Recognition*, pages 5501–5510, 2022. 2
- [15] Qiancheng Fu, Qingshan Xu, Yew Soon Ong, and Wenbing Tao. Geo-NeuS: Geometry-consistent neural implicit surfaces learning for multi-view reconstruction. *Advances in Neural Information Processing Systems*, 35:3403–3416, 2022. 2, 6
- [16] Jingnan Gao, Zhe Wang, Xianze Fang, Xingyu Ren, Zhuo Chen, Shengqi Liu, Yuhao Cheng, Jiangjing Lyu, Xiaokang Yang, and Yichao Yan. More: 3D visual geometry reconstruction meets mixture-of-experts. *Conference on Computer Vision and Pattern Recognition*, 2025. 2
- [17] Stephan J Garbin, Marek Kowalski, Matthew Johnson, Jamie Shotton, and Julien Valentin. FastNeRF: High-fidelity neural rendering at 200fps. In *Proceedings of the IEEE/CVF international conference on computer vision*, pages 14346–14355, 2021. 2
- [18] Jiaming Gu, Minchao Jiang, Hongsheng Li, Xiaoyuan Lu, Guangming Zhu, Syed Afaq Ali Shah, Liang Zhang, and Mohammed Bannamoun. UE4-NeRF: Neural radiance field for real-time rendering of large-scale scene. *Advances in Neural Information Processing Systems*, 36:59124–59136, 2023. 2
- [19] Antoine Guédon and Vincent Lepetit. Sugar: Surface-aligned gaussian splatting for efficient 3D mesh reconstruction and high-quality mesh rendering. In *Proceedings of the IEEE/CVF Conference on Computer Vision and Pattern Recognition*, pages 5354–5363, 2024. 2, 5, 6
- [20] Binbin Huang, Zehao Yu, Anpei Chen, Andreas Geiger, and Shenghua Gao. 2D Gaussian Splatting for Geometrically Accurate Radiance Fields. In *ACM SIGGRAPH 2024 conference papers*, pages 1–11, 2024. 2, 5, 6
- [21] Han Huang, Yulun Wu, Junsheng Zhou, Ge Gao, Ming Gu, and Yu-Shen Liu. NeuSurf: On-surface priors for neural surface reconstruction from sparse input views. In *Proceedings of the AAAI Conference on Artificial Intelligence*, pages 2312–2320, 2024. 2
- [22] Han Huang, Yulun Wu, Chao Deng, Ge Gao, Ming Gu, and Yu-Shen Liu. FatesGS: Fast and accurate sparse-view

- surface reconstruction using gaussian splatting with depth-feature consistency. In *Proceedings of the AAAI Conference on Artificial Intelligence*, 2025. 2
- [23] Rasmus Jensen, Anders Dahl, George Vogiatzis, Engil Tola, and Henrik Aanæs. Large scale multi-view stereopsis evaluation. In *IEEE Conference on Computer Vision and Pattern Recognition*, pages 406–413, 2014. 5
- [24] Haoyi Jiang, Liu Liu, Tianheng Cheng, Xinjie Wang, Tianwei Lin, Zhizhong Su, Wenyu Liu, and Xinggang Wang. GauSSTR: Foundation model-aligned gaussian transformer for self-supervised 3D spatial understanding. In *Proceedings of the Computer Vision and Pattern Recognition Conference*, pages 11960–11970, 2025. 1
- [25] Michael Kazhdan and Hugues Hoppe. Screened poisson surface reconstruction. *ACM Transactions on Graphics (TOG)*, 32(3):1–13, 2013. 2
- [2] Bernhard Kerbl, Georgios Kopanas, Thomas Leimkühler, and George Drettakis. 3D Gaussian Splatting for Real-Time Radiance Field Rendering. *ACM Trans. Graph.*, 42(4):139–1, 2023. 1, 2, 5, 6
- [27] Arno Knapitsch, Jaesik Park, Qian-Yi Zhou, and Vladlen Koltun. Tanks and Temples: Benchmarking large-scale scene reconstruction. *ACM Transactions on Graphics*, 36(4), 2017. 5
- [28] Jiahe Li, Jiawei Zhang, Youmin Zhang, Xiao Bai, Jin Zheng, Xiaohan Yu, and Lin Gu. GeoSVR: Taming sparse voxels for geometrically accurate surface reconstruction. 2
- [29] Qing Li, Huifang Feng, Xun Gong, and Yu-Shen Liu. VA-GS: Enhancing the geometric representation of gaussian splatting via view alignment. In *The Thirty-ninth Annual Conference on Neural Information Processing Systems*, 2025. 1, 2
- [3] Shujuan Li, Yu-Shen Liu, and Zhizhong Han. GaussianUDF: Inferring unsigned distance functions through 3D gaussian splatting. In *Proceedings of the IEEE/CVF Conference on Computer Vision and Pattern Recognition*, 2025. 1, 2, 4, 5, 6
- [31] Zhaoshuo Li, Thomas Müller, Alex Evans, Russell H Taylor, Mathias Unberath, Ming-Yu Liu, and Chen-Hsuan Lin. Neuralangelo: High-fidelity neural surface reconstruction. In *Proceedings of the IEEE/CVF Conference on Computer Vision and Pattern Recognition*, pages 8456–8465, 2023. 2, 5, 6
- [32] Zhihao Liang, Zhangjin Huang, Changxing Ding, and Kui Jia. HelixSurf: A robust and efficient neural implicit surface learning of indoor scenes with iterative intertwined regularization. In *Proceedings of the IEEE/CVF Conference on Computer Vision and Pattern Recognition*, pages 13165–13174, 2023. 2
- [33] Kaimin Liao, Hua Wang, Zhi Chen, Luchao Wang, and Yao-hua Tang. LiteGS: A high-performance framework to train 3DGS in subminutes via system and algorithm codesign. *arXiv preprint arXiv:2503.01199*, 2025. 2
- [34] Jiaqi Liu and Zhizhong Han. Speeding up the learning of 3D gaussians with much shorter gaussian lists. In *Conference on Computer Vision and Pattern Recognition*, 2026. 2
- [35] Yuan Liu, Peng Wang, Cheng Lin, Xiaoxiao Long, Jiepeng Wang, Lingjie Liu, Taku Komura, and Wenping Wang. NeRO: Neural geometry and brdf reconstruction of reflective objects from multiview images. *ACM Transactions on Graphics (TOG)*, 42(4):1–22, 2023. 5
- [36] Xiaoxiao Long, Cheng Lin, Lingjie Liu, Yuan Liu, Peng Wang, Christian Theobalt, Taku Komura, and Wenping Wang. NeuralUDF: Learning Unsigned Distance Fields for Multi-View Reconstruction of Surfaces With Arbitrary Topologies. In *Proceedings of the IEEE/CVF Conference on Computer Vision and Pattern Recognition*, pages 20834–20843, 2023. 2
- [37] William E. Lorensen and Harvey E. Cline. Marching cubes: A high resolution 3D surface construction algorithm. *Computer Graphics*, 21(4):163–169, 1987. 2
- [38] Xiaoyang Lyu, Yang-Tian Sun, Yi-Hua Huang, Xiuzhe Wu, Ziyi Yang, Yilun Chen, Jiangmiao Pang, and Xiaojuan Qi. 3DGSr: Implicit surface reconstruction with 3D gaussian splatting. *ACM Transactions on Graphics (TOG)*, 43(6):1–12, 2024. 2, 4, 5
- [39] Xiaoxu Meng, Weikai Chen, and Bo Yang. NeAT: Learning Neural Implicit Surfaces with Arbitrary Topologies from Multi-view Images. In *Proceedings of the IEEE/CVF Conference on Computer Vision and Pattern Recognition*, pages 248–258, 2023. 2
- [40] Ben Mildenhall, Pratul P Srinivasan, Matthew Tancik, Jonathan T Barron, Ravi Ramamoorthi, and Ren Ng. NeRF: Representing scenes as neural radiance fields for view synthesis. In *European Conference on Computer Vision (ECCV)*, pages 405–421. Springer, 2020. 1, 2, 5, 6
- [41] Thomas Müller, Alex Evans, Christoph Schied, and Alexander Keller. Instant neural graphics primitives with a multiresolution hash encoding. *ACM Transactions on Graphics (TOG)*, 41(4):1–15, 2022. 2, 5, 6
- [42] Michael Oechsle, Songyou Peng, and Andreas Geiger. UNISURF: Unifying neural implicit surfaces and radiance fields for multi-view reconstruction. In *Proceedings of the IEEE/CVF International Conference on Computer Vision*, pages 5589–5599, 2021. 2
- [43] Shiwei Ren, Tianci Wen, Yongchun Fang, and Biao Lu. FastGS: Training 3D gaussian splatting in 100 seconds. *Conference on Computer Vision and Pattern Recognition*, 2025. 2
- [44] Tianchang Shen, Jun Gao, Kangxue Yin, Ming-Yu Liu, and Sanja Fidler. Deep marching tetrahedra: a hybrid representation for high-resolution 3D shape synthesis. *Advances in Neural Information Processing Systems*, 34:6087–6101, 2021. 2
- [45] Cheng Sun, Min Sun, and Hwann-Tzong Chen. Direct voxel grid optimization: Super-fast convergence for radiance fields reconstruction. In *Proceedings of the IEEE/CVF Conference on Computer Vision and Pattern Recognition*, pages 5459–5469, 2022. 2
- [46] Ziyu Tang, Weicai Ye, Yifan Wang, Di Huang, Hujun Bao, Tong He, and Guofeng Zhang. ND-SDF: Learning normal deflection fields for high-fidelity indoor reconstruction. *International Conference on Learning Representations*, 2025. 2
- [47] Matias Turkulainen, Xuqian Ren, Iaroslav Melekhov, Otto Seiskari, Esa Rahtu, and Juho Kannala. Dn-splatter: Depth

- and normal priors for gaussian splatting and meshing. pages 2421–2431, 2025. 2, 5
- [48] Jiepeng Wang, Peng Wang, Xiaoxiao Long, Christian Theobalt, Taku Komura, Lingjie Liu, and Wenping Wang. NeuRIS: Neural reconstruction of indoor scenes using normal priors. In *European conference on computer vision*, pages 139–155. Springer, 2022. 2
- [49] Peng Wang, Lingjie Liu, Yuan Liu, Christian Theobalt, Taku Komura, and Wenping Wang. NeuS: Learning neural implicit surfaces by volume rendering for multi-view reconstruction. *Advances in Neural Information Processing Systems*, 34:27171–27183, 2021. 5, 6
- [50] Yiqun Wang, Ivan Skorokhodov, and Peter Wonka. HF-NeuS: Improved Surface Reconstruction Using High-Frequency Details. *Advances in Neural Information Processing Systems*, 35:1966–1978, 2022. 1, 2
- [51] Yiming Wang, Qin Han, Marc Habermann, Kostas Daniilidis, Christian Theobalt, and Lingjie Liu. NeuS2: Fast learning of neural implicit surfaces for multi-view reconstruction. In *Proceedings of the IEEE/CVF International Conference on Computer Vision*, pages 3295–3306, 2023. 5
- [52] Yaniv Wolf, Amit Bracha, and Ron Kimmel. GS2Mesh: Surface reconstruction from gaussian splatting via novel stereo views. In *European Conference on Computer Vision*, pages 207–224. Springer, 2024. 2
- [53] Qianyi Wu, Jianmin Zheng, and Jianfei Cai. Surface reconstruction from 3d gaussian splatting via local structural hints. In *European Conference on Computer Vision*, pages 441–458. Springer, 2024. 2
- [54] Haofei Xu, Songyou Peng, Fangjinhua Wang, Hermann Blum, Daniel Barath, Andreas Geiger, and Marc Pollefeys. Depthsplat: Connecting gaussian splatting and depth. In *Proceedings of the Computer Vision and Pattern Recognition Conference*, pages 16453–16463, 2025. 1
- [55] Lior Yariv, Jiatao Gu, Yoni Kasten, and Yaron Lipman. Volume rendering of neural implicit surfaces. *Advances in Neural Information Processing Systems*, 34:4805–4815, 2021. 5, 6
- [56] Lior Yariv, Peter Hedman, Christian Reiser, Dor Verbin, Pratul P Srinivasan, Richard Szeliski, Jonathan T Barron, and Ben Mildenhall. BakedSDF: Meshing neural sdf for real-time view synthesis. In *ACM SIGGRAPH 2023 Conference Proceedings*, pages 1–9, 2023. 5, 6
- [57] Mulin Yu, Tao Lu, Linning Xu, Lihan Jiang, Yuanbo Xiangli, and Bo Dai. GSDF: 3DGS meets sdf for improved neural rendering and reconstruction. *Advances in Neural Information Processing Systems*, 37:129507–129530, 2024. 2, 5, 6
- [58] Zehao Yu, Songyou Peng, Michael Niemeyer, Torsten Sattler, and Andreas Geiger. MonoSDF: Exploring monocular geometric cues for neural implicit surface reconstruction. *Advances in neural information processing systems*, 35:25018–25032, 2022. 6
- [59] Zehao Yu, Torsten Sattler, and Andreas Geiger. Gaussian Opacity Fields: Efficient adaptive surface reconstruction in unbounded scenes. *ACM Transactions on Graphics (TOG)*, 43(6):1–13, 2024. 2, 4, 5, 6, 7
- [60] Baowen Zhang, Chuan Fang, Rakesh Shrestha, Yixun Liang, Xiao-Xiao Long, and Ping Tan. Rade-GS: Rasterizing depth in gaussian splatting. *ACM Transactions on Graphics*, 2024. 2
- [61] Jingyang Zhang, Yao Yao, Shiwei Li, Tian Fang, David McKinnon, Yanghai Tsin, and Long Quan. Critical regularizations for neural surface reconstruction in the wild. In *Proceedings of the IEEE/CVF Conference on Computer Vision and Pattern Recognition*, pages 6270–6279, 2022. 2
- [62] Wenyuan Zhang, Jimin Tang, Weiqi Zhang, Yi Fang, Yu-Shen Liu, and Zhizhong Han. MaterialRefGS: Reflective gaussian splatting with multi-view consistent material inference. 1
- [4] Wenyuan Zhang, Yu-Shen Liu, and Zhizhong Han. Neural signed distance function inference through splatting 3D gaussians pulled on zero-level set. In *Advances in Neural Information Processing Systems*, 2024. 1, 2, 4, 5, 6, 7
- [64] Wenyuan Zhang, Chunsheng Wang, Kanle Shi, Yu-Shen Liu, and Zhizhong Han. VRP-UDF: Towards unbiased learning of unsigned distance functions from multi-view images with volume rendering priors. *IEEE Transactions on Pattern Analysis and Machine Intelligence*, 2026. 2
- [5] Ziyu Zhang, Binbin Huang, Hanqing Jiang, Liyang Zhou, Xiaojun Xiang, and Shuhan Shen. Quadratic Gaussian Splatting: High quality surface reconstruction with second-order geometric primitives. In *Proceedings of the IEEE/CVF International Conference on Computer Vision*, pages 28260–28270, 2025. 5, 6, 7, 1
- [66] Junsheng Zhou, Weiqi Zhang, Baorui Ma, Kanle Shi, Yu-Shen Liu, and Zhizhong Han. UDFStudio: A unified framework of datasets, benchmarks and generative models for unsigned distance functions. *IEEE Transactions on Pattern Analysis and Machine Intelligence*, 2026. 2
- [67] Xingxing Zuo, Pouya Samangouei, Yunwen Zhou, Yan Di, and Mingyang Li. FMGS: Foundation model embedded 3D gaussian splatting for holistic 3D scene understanding. *International Journal of Computer Vision*, 133(2):611–627, 2025. 1

3D Gaussian Splatting with Self-Constrained Priors for High Fidelity Surface Reconstruction

Supplementary Material

1. Implementation Details

We follow 3DGS [2] in the experimental setting. We adopt the same optimization schedule to train 30000 iterations with Adam optimizer and start from randomly initialized Gaussian attributes. The TSDF grid f^t is updated every 5000 iterations up to iteration 20000. The bandwidth scaling is set to 1, 0.5, 0.25 in each updated f^t , respectively. We enable L_{SCP} at 10000 iteration and use a decision threshold $\delta^t = 0.3$ on f^t to label Gaussians for L_{SCP} . All experiments run on a single NVIDIA RTX 4090 GPU.

2. Optimization Details

Rendering Losses. During rendering optimization, we supervise the learning of 3D Gaussians using a unified image reconstruction loss L_{RGB} , which comprises three components: a MAE loss L_{MAE} that constrains pixel-level differences, a SSIM loss L_{SSIM} that preserves structural consistency, and a NCC loss L_{NCC} that enforces multi-view consistency. Together, these terms enable the model to achieve accurate color reconstruction, maintain structural fidelity, and ensure geometric consistency across views.

$$L_{RGB} = (1 - \beta)L_{MAE}(v_{gt}, v_{pred}) + \beta L_{SSIM}(v_{gt}, v_{pred}) + (1 - L_{NCC}(v_r(h_r), v_n(H_{rm}h_r))), \quad (11)$$

where β is the balance weight. v_{gt} and v_{pred} denote the ground-truth and rendered views, respectively. v_r and v_n represent the reference and target views. h_r is the homogeneous pixel coordinate in the reference view, and H_{rm} is the corresponding homography matrix.

Signed Distance Inference for 3D Gaussians. As described in Sec. 3.1, unlike previous methods that fit an implicit field from Gaussian points, we predict the signed distance for each Gaussian point $q_i = [x_i, y_i, z_i]$ using the implicit prior f^t . We efficiently interpolate the distance using trilinear interpolation,

$$f^t(q_i) = a_0 + a_1x_i + a_2y_i + a_3z_i + a_4x_iy_i + a_5x_iz_i + a_6y_iz_i + a_7x_iz_i, \quad (12)$$

where $\{a_0, \dots, a_7\}$ are the interpolation weights of the TSDF grid vertices surrounding q_i .

3. More Comparisons and Results

In this subsection, we conduct additional ablation studies on the DTU dataset under the default parameter settings and

provide more visual results and comparisons on both synthetic and large-scale scene datasets.

Effect of Opacity Constraint Threshold. We analyze the effect of the opacity constraint threshold δ^t on splitting 3D Gaussians into on-surface and off-surface subsets. Specifically, we add noise to surface points to evaluate the accuracy of f^t under different thresholds. We set δ^t to 0.7, 0.5, 0.3, and 0.1, respectively. As shown in Fig. 13, a lower value of δ^t makes Gaussians more sensitive to be classified as off-surface points, while the higher ones relax the threshold but decreases the supervision accuracy. We further visualize the Gaussian classification results of f^t under different settings. When δ^t is set to 0.1, most on-surface points are incorrectly labeled as outliers. In contrast, f^t tends to label outliers as surface points as δ^t is higher than 0.3. To balance robustness and accuracy, we set δ^t to 0.3 by default.

Visual Comparisons on NeRF-Synthetic. We provide additional comparisons in Fig. 14. compared with implicit-field-based approaches (GS-Pull [4] and GS-UDF [3]), our method reconstructs more complete surfaces in open-surface scenarios. In contrast to TSDF based methods (QGS [5] and PGSR [1]), our approach leverages geometric priors to better preserve edge structures and reduce outliers and truncation artifacts on the boat hull or plate. Our method also recovers local details in scenes with complex textures. We further provide serial rendering visualization and evaluation in our video.

Visualization on DTU. We also present qualitative results on the DTU dataset in Fig. 15. As shown in Fig. 15, our method recovers more accurate surfaces in regions with complex geometric topology and maintains consistency across various open scenes.

Visualization on TNT and Mip-NeRF 360. We further validate the geometry inference and novel view rendering performance for our method on large-scale scenes (TNT and Mip-NeRF 360) in Fig. 16 and Fig. 17. As shown in Fig. 16, our method recovers accurate geometric structures in both complex indoor and outdoor environments. Moreover, we produce high-fidelity rendered views under low-texture regions and challenging lighting conditions in Fig. 17.

4. Optimization Terms Explanation

Mean Absolute Error (MAE). SSIM evaluates the perceptual similarity between two views considering contrast and structure. Given the ground-truth view v_{gt} and the predicted view v_{pred} , the MAE loss computes the average absolute

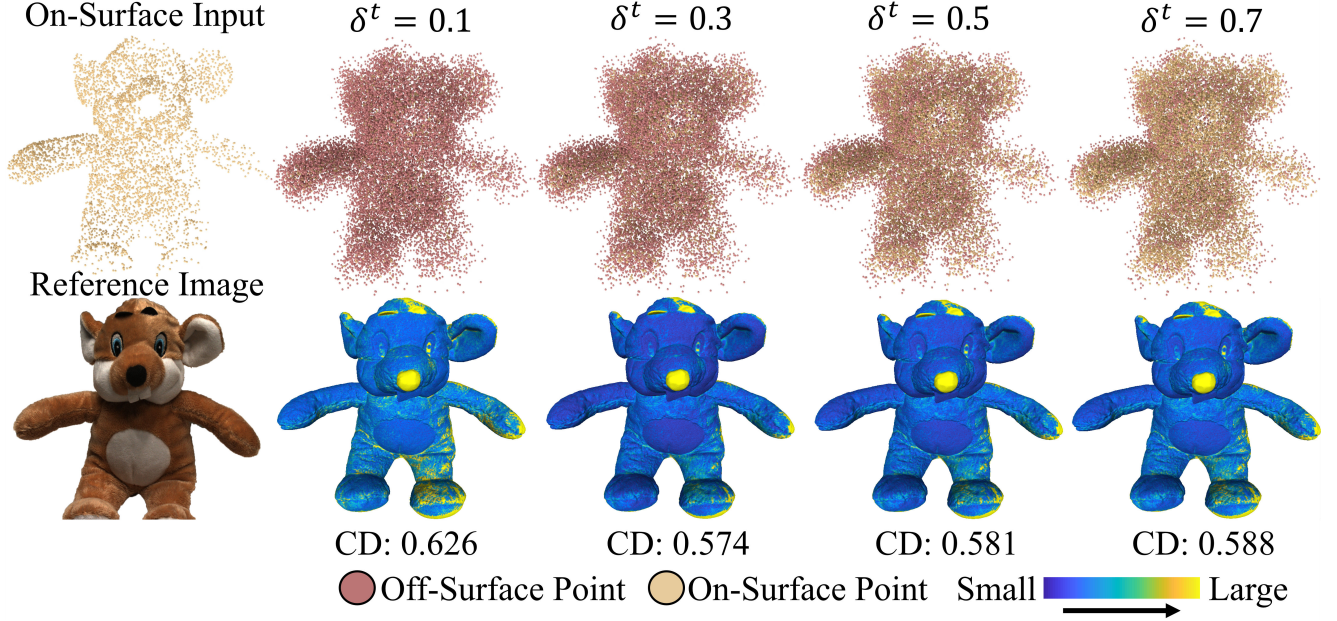


Figure 13. Effect of Opacity Constraint Threshold.

pixel-wise difference and is formulated as,

$$L_{MAE}(v_{gt}, v_{pred}) = |v_{gt} - v_{pred}|. \quad (13)$$

Structural Similarity (SSIM). SSIM evaluates the perceptual similarity between two views considering luminance, contrast, and structure. Given the ground-truth view v_{gt} and the predicted view v_{pred} , the SSIM is defined as,

$$L_{SSIM}(v_{gt}, v_{pred}) = \frac{(2\mu_{gt}\mu_{pred} + T_1)(2\sigma_{gt,pred} + T_2)}{(\mu_{gt}^2 + \mu_{pred}^2 + T_1)(\sigma_{gt}^2 + \sigma_{pred}^2 + T_2)}, \quad (14)$$

where μ_{gt} and μ_{pred} are means, σ_{gt}^2 and σ_{pred}^2 are the variances, $\sigma_{gt,pred}$ is the covariance between v_{gt} and v_{pred} , T_1 and T_2 are constants.

Normalized Cross-Correlation (NCC). NCC measures the linear correlation between two views after removing their mean intensities. Given the ground-truth view v_{gt} and the predicted view v_{pred} , the NCC is defined as,

$$L_{NCC}(v_{gt}, v_{pred}) = \frac{\sum_{i=1}^N (v_{gt}^{(i)} - \mu_{gt})(v_{pred}^{(i)} - \mu_{pred})}{\sqrt{\sum_{i=1}^N (v_{gt}^{(i)} - \mu_{gt})^2} \sqrt{\sum_{i=1}^N (v_{pred}^{(i)} - \mu_{pred})^2}}, \quad (15)$$

where i is the pixel index and N is the total number of pixels. μ_{gt} and μ_{pred} denote the mean intensities of all pixels in v_{gt} and v_{pred} , respectively.

5. Codes

We provide a demonstration code as a part of our supplementary materials. We will release the source code and data upon acceptance.

6. Video

We provide a video containing the visualizations on all datasets as a part of our supplementary materials.

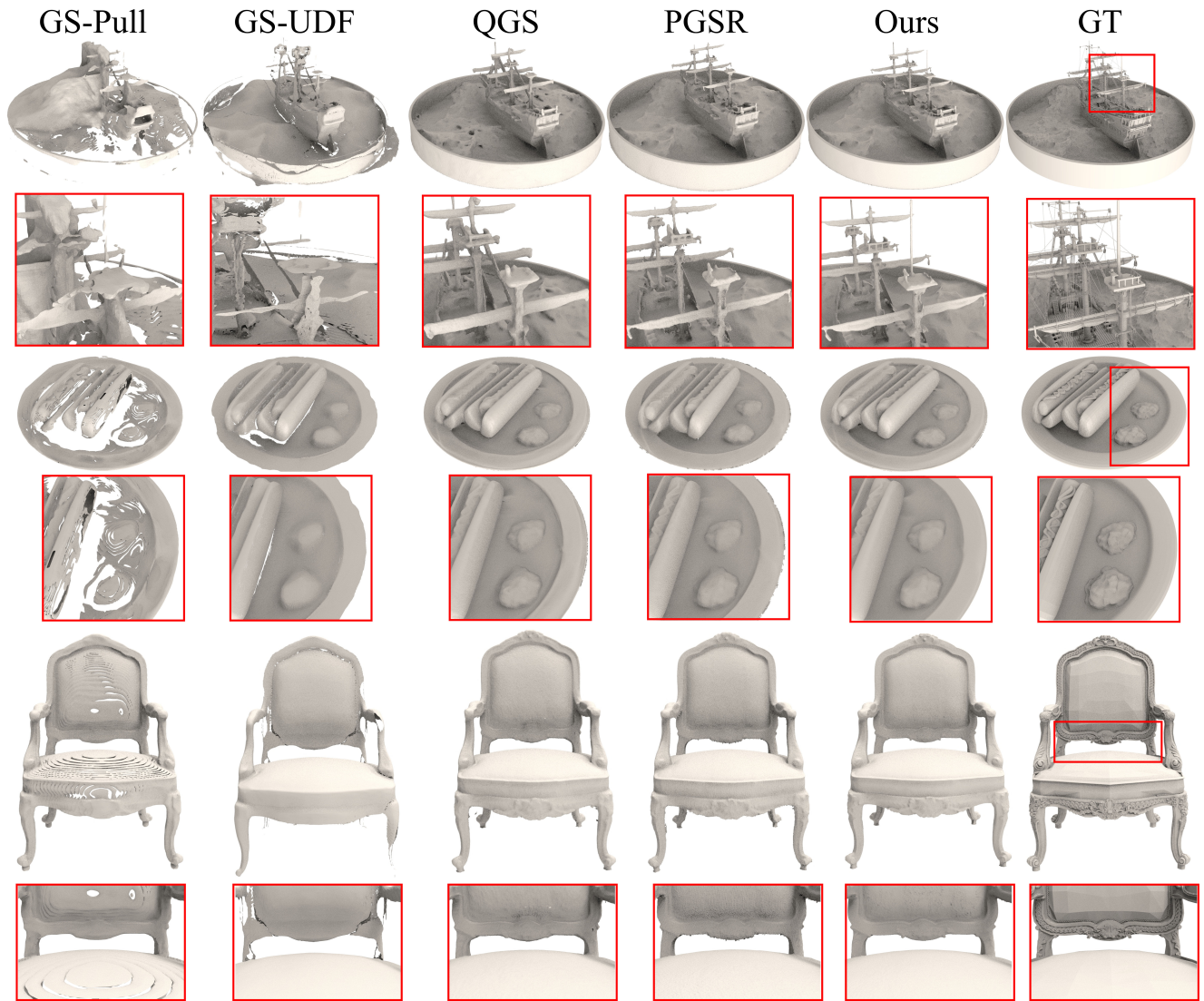


Figure 14. Visual Comparisons on NeRF-Synthetic Dataset.



24



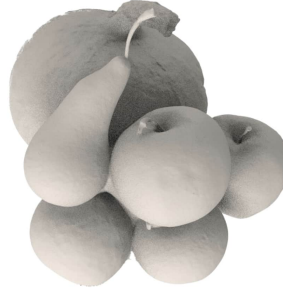
37



40



55



63



65



69



83



97



105



106



110



114



118



122

Figure 15. Visual Comparisons on DTU Dataset.



Figure 16. Surface Reconstruction Visualization on TNT and Mip-NeRF 360 Dataset.

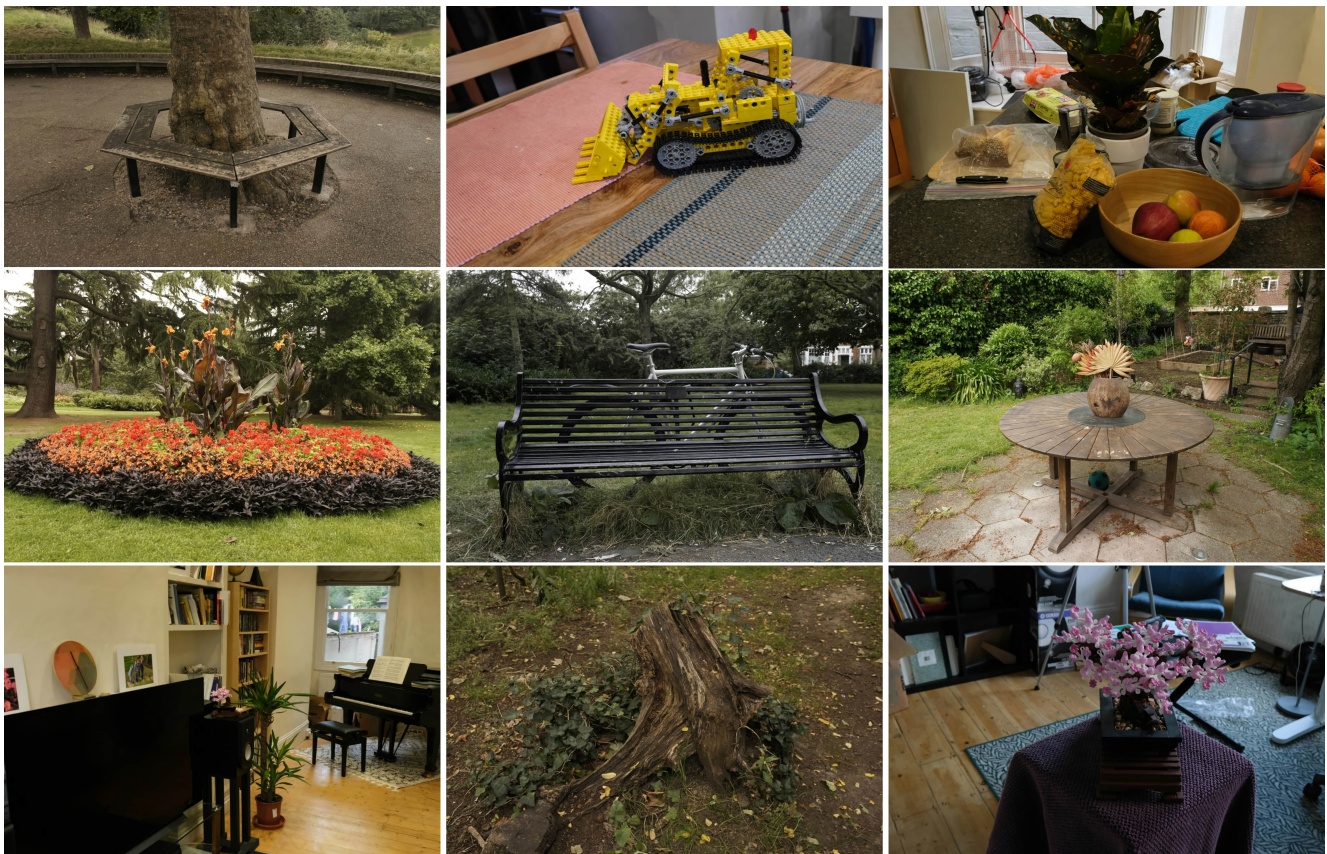


Figure 17. Rendering Visualization on Mip-NeRF 360 Dataset.

References

- [1] Danpeng Chen, Hai Li, Weicai Ye, Yifan Wang, Weijian Xie, Shangjin Zhai, Nan Wang, Haomin Liu, Hujun Bao, and Guofeng Zhang. PGSR: Planar-based gaussian splatting for efficient and high-fidelity surface reconstruction. *IEEE Transactions on Visualization and Computer Graphics*, 2024. [1](#), [2](#), [5](#), [6](#), [7](#)
- [2] Bernhard Kerbl, Georgios Kopanas, Thomas Leimkühler, and George Drettakis. 3D Gaussian Splatting for Real-Time Radiance Field Rendering. *ACM Trans. Graph.*, 42(4):139–1, 2023. [1](#), [2](#), [5](#), [6](#)
- [3] Shujuan Li, Yu-Shen Liu, and Zhizhong Han. GaussianUDF: Inferring unsigned distance functions through 3D gaussian splatting. In *Proceedings of the IEEE/CVF Conference on Computer Vision and Pattern Recognition*, 2025. [1](#), [2](#), [4](#), [5](#), [6](#)
- [4] Wenyuan Zhang, Yu-Shen Liu, and Zhizhong Han. Neural signed distance function inference through splatting 3D gaussians pulled on zero-level set. In *Advances in Neural Information Processing Systems*, 2024. [1](#), [2](#), [4](#), [5](#), [6](#), [7](#)
- [5] Ziyu Zhang, Binbin Huang, Hanqing Jiang, Liyang Zhou, Xiaojun Xiang, and Shuhan Shen. Quadratic Gaussian Splatting: High quality surface reconstruction with second-order geometric primitives. In *Proceedings of the IEEE/CVF International Conference on Computer Vision*, pages 28260–28270, 2025. [5](#), [6](#), [7](#), [1](#)